An Inverter-Nonlinearity-Immune Offline Inductance Identification Method for PMSM Drives Based on Equivalent Impedance Model

Qiwei Wang, Gaolin Wang, *Senior Member, IEEE*, Shaobo Liu, Guoqiang Zhang, *Member, IEEE*, and Dianguo Xu, *Fellow, IEEE*

***Abstract*—In the existing offline inductance identification methods of permanent magnet synchronous machines (PMSMs), *dq*-axis voltage equations are generally adopted and the inverter nonlinearity compensation is necessary, which complicates the identification process and restricts the generality. In order to solve the problem, an offline inverter-nonlinearity-immune inductance identification method is proposed in this article based on the PMSM equivalent impedance model. The method can identify the *dq*-axis inductances by injecting both dc and high frequency signals, where the magnetic saturation and the cross saturation are considered. Besides, an inductance surface forming algorithm is introduced based on the bilinear interpolation. The continuous *dq*-axis inductance surfaces can be then obtained by only a few identified data, so that the time of data sampling and processing is greatly shorten compared with the existing methods. To enhance the accuracy of the identification method, the digital delay error and the sampling error in zero current zone are investigated and compensated. The effectiveness of the proposed method is validated on three different test machines.**

***Index Terms*—Digital delay effect, equivalent impedance model, offline inductance identification, permanent magnet synchronous motor (PMSM), sampling error in zero current zone (ZCZ).**

I. Introduction

PERMANENT magnet synchronous machines (PMSMs) have been widely applied in industrial fields for the high power density, good performances, and flexible controllability [1]–[4]. In PMSM applications, machine parameters are essential to almost all kinds of control schemes [5]–[8]. Besides, the parameters can also be used to the machine state monitoring, the fault diagnosing, etc. [9]–[13]. Given the importance of machine parameters, the identification methods have been widely investigated in recent years. According to the applicable working conditions, parameter identification methods can be divided into online and offline methods [5], [6]. The offline parameter identification methods, for not affecting the online operation condition and saving control resources, have attracted wide spread concern from both industry and academia over the past few years [3], [4]. As one of the most important and difficult parts of the offline identification process, offline inductance identification deserves to be studied deeply.

Offline inductance identification is supposed to obtain the inductance surface under different *dq*-axis current combinations at standstill [16] so that it can be applied in different control schemes at varying operating conditions. In [6] and [17], the offline inductance identification method based on the high frequency (HF) square wave injection was introduced. *dq*-axis inductances are calculated by the differential operation of the *dq*-axis flux linkages estimated in advance by the hysteresis control of *dq*-axis currents. In [7], a magnetic model self-identification (MMSI) technique was presented to evaluate the *dq* flux linkages, considering the magnetic saturation and the cross-coupling effect, with the rotor shaft left free and current controlled. An amplitude-auto-adjusting signal injection method based on the hysteresis control was researched to realize the inductance identification [16]. In addition to the voltage-equation-based methods, in [14] and [15], the sinusoidal current injection based method was proposed, where the *dq*-axis inductances are calculated by the information of the injected currents and the induced voltages. Since the signals need to be injected into the actual *dq* axes [14], [15], the rotor position should be measured through the encoder. Moreover, the rotor shaft locking might be needed to prevent the undesired rotor rotation when the amplitude of the injected signals is high [6], [17].

Even though the voltage equation based methods have been most widely used, the inevitable inverter nonlinearity largely limits the generality of the methods by introducing a voltage error varying with the current [19]–[21]. In order to solve the problem, the sign function was applied to compensate the inverter nonlinearity error [19]. For better simulating the inverter nonlinearity in inductance identification at low current, the trapezoidal voltage compensation was utilized [20]. In [18], the inverter nonlinearity was described by the mathematical fitting formula, which better compensates the inverter nonlinearity in inductance identification. In [16], a self-learning method based

Manuscript received July 7, 2021; revised October 30, 2021; accepted December 24, 2021. Date of publication December 28, 2021; date of current version February 18, 2022. This work was supported in part by the Research Fund for the National Natural Science Foundation of China under Grants 52125701 and 52177034, and in part by the Fundamental Research Funds for the Central Universities under Grant FRFCU5710092020. Recommended for publication by Associate Editor T. Shi. *(Corresponding author: Gaolin Wang.)*

The authors are with the School of Electrical Engineering and Automation, Harbin Institute of Technology, Harbin 150001, China (e-mail: wqw0543@163.com; wgl818@hit.edu.cn; liushaobohit@163.com; zhgq@hit.edu.cn; xudiang@hit.edu.cn).

Color versions of one or more figures in this article are available at https://doi.org/10.1109/TPEL.2021.3138886.

Digital Object Identifier 10.1109/TPEL.2021.3138886

on the Hermite interpolation was proposed, which could realize the accurate inverter nonlinearity compensation. However, the inverter nonlinearity effect is too complex to be accurately compensated only by the sign function or the fitting formula [16]. The self-learning method can meet the compensation accuracy, but additional process is required. In sum, the inverter nonlinearity compensation is still one of the major difficulties of existing voltage equation based methods.

Furthermore, since the existing methods [16], [17] calculate *dq*-axis inductances through the flux linkage, a large amount of intermediate data needs to be estimated and stored in the controller. Then, a great amount of partial differential operation based on the stored flux linkage data is needed for the *dq*-axis inductance identification [16], [18]. At the same time, for ensuring that the inductance surface covers as many working conditions as possible, more data should be sampled under more *dq*-axis current combinations [22]. In this case, the existing voltage equation based offline identification methods are resource- and time-consuming.

Since the signal injection is necessary for the offline inductance identification methods, the identification errors come from many aspects [6]. In [23], the effect of the HF injected signal on the machine saturation state, determining the inductance value, was studied. As the voltage source inverter is generally applied in the parameter identification, the sampling errors in the current and voltage are inevitable [24], [25], which need to be investigated and compensated. In [18], the identification error caused by the abc-phase zero current clamping effect was analyzed and compensated by choosing the proper signal injection amplitude. In [26] and [27], it was shown that with the HF signal injection, the digital delay effect on the parameter identification should be considered. In sum, the identification errors need to be carefully analyzed and compensated.

For dealing with the limitations of the existing methods, an inverter-nonlinearity-immune offline inductance identification method is introduced as follows. First, the equivalent impedance model is introduced based on the PMSM physical model. On this basis, the proposed inductance identification method is explained in detail, together with the advantages over the existing voltage equation based methods. Furthermore, the bilinear interpolation based inductance surface forming method is studied, which can obtain the continuous inductance surface from only a few discrete data. Meanwhile, for ensuring the identification accuracy, the digital delay effect and the sampling error in zero current zone (ZCZ) on the inductance identification are analyzed and compensated. Finally, the experimental results on three test machines are presented show good identification effect, which are compared by the identification method in [17] and verified by the identification method in [23].

The rest of this article is organized as follows. In Section II, the equivalent impedance model and the offline inductance identification method are introduced, along with the bilinear interpolation based inductance surface forming algorithm. In Section III, the digital delay error and the sampling error in ZCZ is analyzed and compensated. Experimental results of three test machines are presented in Section IV. Finally, Section V concludes this article.

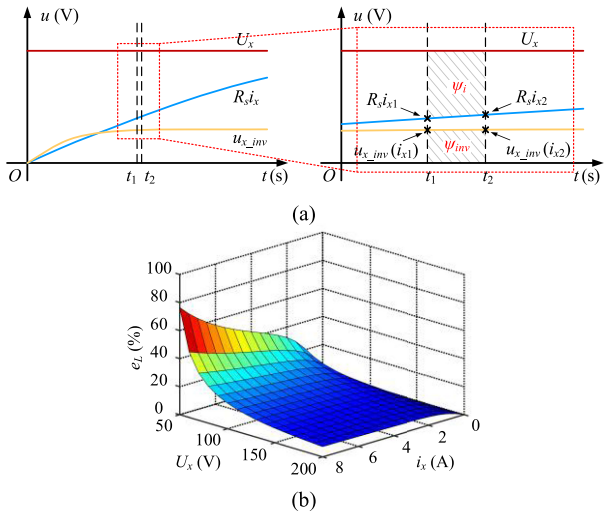

Fig. 1. Effect of inverter nonlinearity on inductance identification of (1). (a) Effect of inverter nonlinearity error voltage. (b) Surface of inductance error verses amplitude of injected voltage and induced current.

II. Proposed Offline Inductance Identification Method Based on Equivalent Impedance Model

A. PMSM Equivalent Impedance Model for Inductance Identification

The existing offline inductance identification methods are mostly based on the voltage equation and carried out by HF square voltage injection. The *dq*-axis inductances are calculated from the differential operation of the flux linkage identified in advance, which is shown as follows:

$$\begin{cases} u_x = \frac{\mathrm{d}\psi_x}{\mathrm{d}t} + R_s i_x + u_{x\_\mathrm{inv}} \\ L_x = \frac{\mathrm{d}\psi_x}{\mathrm{d}i_x} = \frac{\mathrm{d}}{\mathrm{d}i_x}\int (u_x - u_{x\_\mathrm{inv}} - R_s i_x)\, dt \end{cases} \quad x = d, q \quad (1)$$

where $u_{d,q}$ are the *dq*-axis voltages, $i_{d,q}$ are the *dq*-axis currents, and $L_{d,q}$ is the *dq*-axis inductances. R_s is the stator resistance and $\psi_{d,q}$ is the *dq*-axis flux linkages. u_{d,q_inv} is the voltage error caused by inverter nonlinearity. It should be noted that u_{d,q_inv} is generally unknown in the identification process. Based on the existing literatures [16], [18], u_{d,q_inv} introduces a nonlinear error into the output voltage, which varies with the current. In the conventional method, the effect of u_{d,q_inv} on the parameter identification is analyzed as follows.

As shown in Fig. 1, the square wave injection is applied, where $U_{d,q}$ is the amplitude of the injected voltage. During the injection, the current and the corresponding u_{d,q_inv} are also illustrated in Fig. 1(a). Since the actual pulsewidth modulation (PWM) control is discrete, in the small time interval $t_1 - t_2$, (1) can be rewritten by the discrete form shown as follows:

$$\begin{cases} \psi_{x2} - \psi_{x1} = \Delta\psi_x = (U_x - u_{x\_\mathrm{inv}} - R_s i_{x\_\mathrm{avg}})\Delta t \\ L_x(i_{x\_\mathrm{avg}}) = (\psi_{x2} - \psi_{x1})/(i_{x2} - i_{x1}) \\ \quad = (U_x - u_{x\_\mathrm{inv}} - R_s i_{x\_\mathrm{avg}})\Delta t/(i_{x2} - i_{x1}) \end{cases} \quad x = d, q \quad (2)$$

where Δt is equal to $t_2 - t_1$. $\Delta\psi_{d,q}$ is the flux linkage change in Δt, equal to $\psi_i - \psi_{\mathrm{inv}}$ in Fig. 1(a). i_{d,q_avg} is the average current in the whole Δt. Since Δt is small, i_{d,q_avg} is approximately

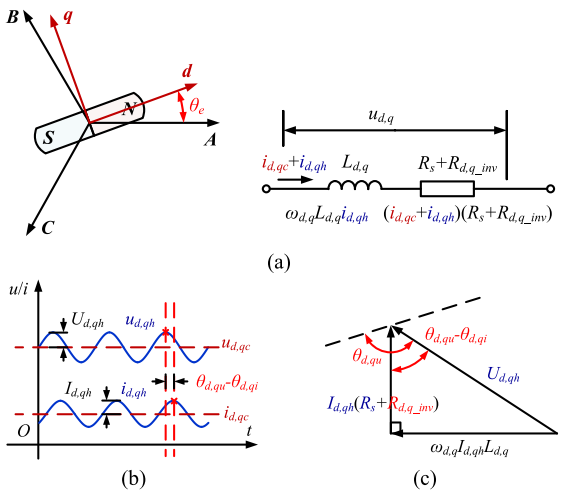

Fig. 2. Equivalent impedance model of PMSM. (a) Physical model of PMSM. (b) Sinusoidal response of equivalent impedance model. (c) Vector form of equivalent impedance model.

equal to $(i_{d,q1} + i_{d,q2})2$. The identification error e_L of the inverter nonlinearity on the identified $L_{d,q}$ can be then expressed by

$$e_L(i_x, U_x) = \frac{L_x - L_{x\_\mathrm{err}}}{L_x} = \frac{u_{x\_\mathrm{inv}}}{U_x} - u_{x\_\mathrm{inv}} - R_s i_{x\_\mathrm{avg}} x = d, q. \tag{3}$$

The value of u_{d,q_inv} of the test inverter is simulated by the mathematical function in [18], the effectiveness of which has been proved. The overall error on the identified inductance e_L is presented in Fig. 1(b). When u_{d,q_inv} is not compensated, the higher the $U_{d,q}$ is, the less the e_L will be. When $i_{d,q}$ is higher than 2 A, the inverter nonlinearity error is higher than 10%.

Considering the characteristics of the voltage equation based methods, two restrictions would limit the generality of the existing methods, which are explained as follows.

1) The offline inductance identification methods based on the voltage equation are inevitably affected by u_{d,q_inv}. Hence, the inverter nonlinearity should be compensated, which greatly complicates the identification process.
2) Since the flux linkage is the essential results in the voltage equation based methods, a large amount of intermediate data have to be stored, and a lot of differential operation needs to be carried out for calculating $L_{d,q}$, which is resource consuming.

For dealing with the disadvantages, an offline inductance identification method based on the equivalent impedance model is investigated. Based on the physical model of PMSM, the abc-phase and *dq*-axis circuits can be seen as a serial combination of an ideal resistor and an ideal inductor, as shown in Fig. 2, which is reasonably named "equivalent impedance model." In Fig. 2(a) and (b), the response signals of the equivalent impedance model under HF sinusoidal voltage injection and dc current injection contain the parameters, which can be expressed by (4), where the subscripts "*c*" and "*h*" represent the injected dc signal and HF signal, respectively.

$U_{d,qh}$ and $I_{d,qh}$ are the amplitude of the HF injected sinusoidal voltages and the induced currents, respectively, in Fig. 2(b). $\theta_{d,qu}$ and $\theta_{d,qi}$ are the initial phase angles of the HF voltage and current, respectively. Since the inverter nonlinearity is corresponding to the current at real time without any signal exceeding or lagging, it can be represented as an equivalent resistance R_{d,q_inv} in Fig. 2(c) [18], which is equal to u_{d,q_inv} / $i_{d,q}$ coinciding with the resistance vector [16], [23]

$$\begin{cases} u_x = u_{xc} + u_{xh} + u_{x\_\mathrm{inv}} \\ u_{xc} = R_s i_{xc} \\ u_{xh} = U_{xh} e^{j(\omega_x t + \theta_{xu})} = j\omega_x L_x i_{xh} + R_s i_{xh} \\ \quad = \omega_x L_x I_{xh} e^{j(\omega_x t + \theta_{xi} + \frac{\pi}{2})} + R_s I_{xh} e^{j(\omega_x t + \theta_{xi})} \end{cases} x = d, q\ . \tag{4}$$

When injecting the HF sinusoidal voltage, the vector form of the equivalent impedance model is shown in Fig. 2(c). The modes of the vectors, $U_{d,qh}$ and $I_{d,qh}$, are equal to the amplitudes of the sinusoidal voltage and current, respectively. $\omega_{d,q} I_{d,qh} L_{d,q}$ and $I_{d,qh} R_s$ are the inductive and resistive components. θ_e is the angle between *a*-phase and *d*-axis.

It can be found out from the impedance vector that the inductive component and the resistive component, along with the inverter nonlinearity component, are completely decoupled [23]. Since the machine is standstill in the offline identification, the inverter nonlinearity voltage error and the equivalent resistance are not affected by the sixth harmonic pulsation versus the rotor position.

B. Offline Inductance Identification Method Based on Equivalent Impedance Model

The proposed offline inductance identification method is achieved by injecting both dc signal and HF sinusoidal signal. Since the rotor is stand still, the injected HF signal is the only ac signal in the identification process. As shown in Fig. 2 and (4), the dc response and the HF sinusoidal response in the equivalent impedance model can be analyzed independently, and the $L_{d,q}$ are only contained in the HF sinusoidal response. Hence, in the proposed method, dc signal injection is applied to set the specific PMSM saturation state and HF signal is to estimate inductance.

Through the impedance relationship in Fig. 2, $L_{d,q}$ can be estimated with HF sinusoidal voltage injection, and the PMSM saturation state is determined by injecting certain *dq*-axis dc currents. The injected HF sinusoidal voltage and the induced HF current are involved in the HF equivalent impedance model as the real part Re[] of the voltage and current vectors, which are presented as follows:

$$\begin{cases} u_{xh} = \mathrm{Re}[U_{xh} e^{j(\omega_x t + \theta_{ud})}] = U_{xh} cos\,(\omega_x t + \theta_{ux}) \\ i_{xh} = \mathrm{Re}[I_{xh} e^{j(\omega_x t + \theta_{id})}] = I_{xh} cos\,(\omega_x t + \theta_{ix}) \end{cases} x = d, q. \tag{5}$$

As shown in Fig. 2(c), the inductance can be calculated by the mathematical relationship between the amplitude and initial phase of $u_{d,qh}$ and $i_{d,qh}$ in the equivalent impedance model. Since the $L_{d,q}$ identification process only concern the certain saturation point determined by the dc current references, the inductance identified in this article is the differential inductance.

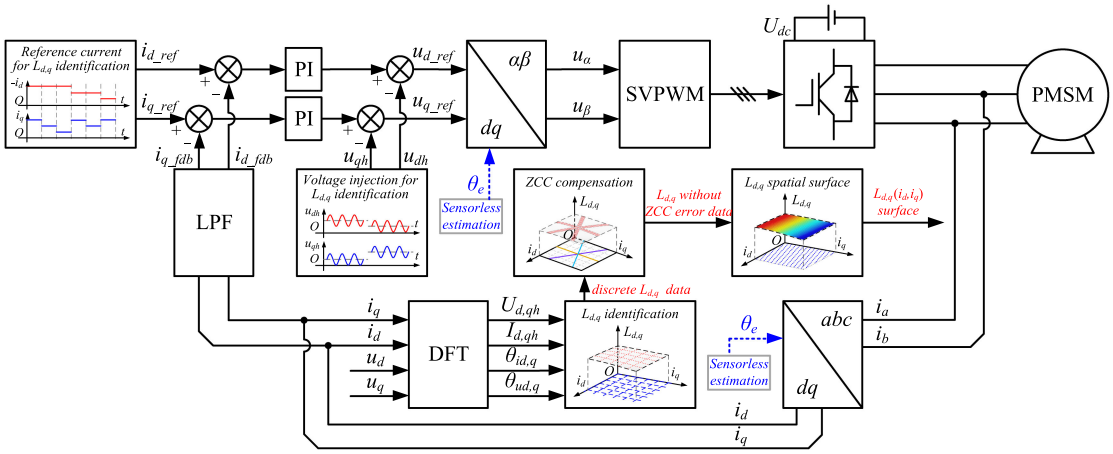

Fig. 3. Block diagram of the proposed offline inductance identification process.

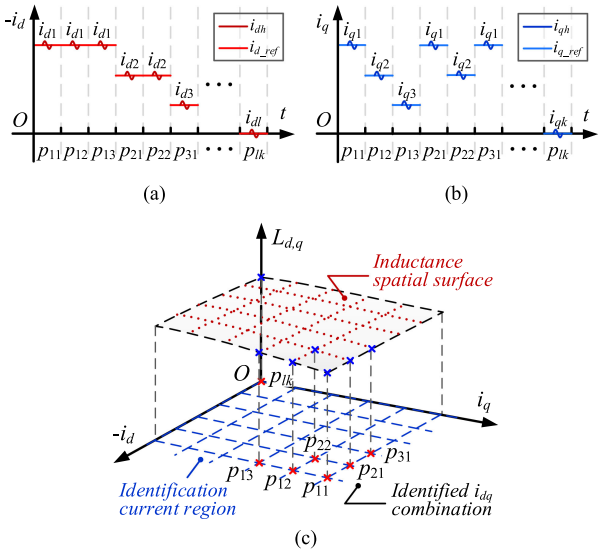

Fig. 4. Proposed signal injection method and surface forming algorithm in inductance identification process. (a) *d*-axis current injection scheme. (b) *q*-axis current injection scheme. (c) Identified points in the inductance surface.

The mathematical expressions of the PMSM inductance, along with the resistive component can be written as follows:

$$\begin{cases} L_x = \mathrm{Im}[\frac{u_{xh}}{\omega_x i_{xh}}] = \frac{U_{xh}}{\omega_x I_{xh}} \sin(\theta_{xu} - \theta_{xi}) \\ R_s + R_{inv} = Re[\frac{u_{xh}}{\omega_x i_{xh}}] = \frac{U_{xh}}{I_{xh}} cos(\theta_{xu} - \theta_{xi}) \end{cases} \quad x = d, q. \tag{6}$$

The inductance is contained in the imaginary part Im[] of the impedance vector. According to (6), $L_{d,q}$ terms are completely decoupled from the resistive components in the real part Re[], where the inverter nonlinearity term R_{d,q_inv} is included. In the $L_{d,q}$ calculation process, only the amplitudes and the phases of the *dq*-axis currents and voltages are involved. Since the equivalent resistance, along with the inverter nonlinearity, need not be concerned at all, the immunity of the inverter nonlinearity error can be then realized. The discrete Fourier transform (DFT) is adopted to estimate the amplitude and initial phase information of $u_{d,q}$ and $i_{d,q}$, $U_{d,qh}$, $I_{d,qh}$, $\theta_{d,qu}$, and $\theta_{d,qi}$, as shown in (7), where $N_{d,q}$ are the numbers of PWM period in one injected sinusoidal injection period of dq axes. Under each current level, the DFT processing is identical and the processing time is constant.

The whole inductance identification process is shown in Fig. 3. The dc current injection is carried out first with certain *dq*-axis current references i_{d,q_ref}, on which the HF sinusoidal voltage $u_{d,qh}$ are injected additionally to estimate the *dq*-axis inductance. The identification can be carried out at both the nonlinear and the linear part of the inverter nonlinearity. $U_{d,qh}$ should be small so as not to change the preset saturation state of PMSM. In experimental tests, the value 0.01 p.u. is enough to achieve good identification effect. As for the injection frequency, $N_{d,q}$ should be chosen from 10 to 20 to guarantee the extraction accuracy of DFT. The *dq*-axis injection frequencies should be different to avoid the coupling of the extracted information of dq axes. The frequencies of the injected HF *dq*-axis voltages are selected as 300 and 375 Hz. During the identification process, the rotor shaft should be locked to keep the motor at standstill.

C. Inductance Surface Forming Algorithm Based on Bilinear Interpolation

In order to consider the magnetic saturation and cross saturation, the offline inductance identification method is supposed to identify the $L_{d,q}$ surfaces under different $i_{d,q}$ combinations [16]. In the existing voltage equation based methods, the $L_{d,q}$ surfaces under different $i_{d,q}$ are obtained by adjusting the amplitude of the injected signals based on the hysteresis control [17]. In order to form the continuous $L_{d,q}$ surfaces from the discrete identification points, the sampled data in the existing methods should be increased as many as possible, which is resource- and time-consuming. In order to solve the problem, a surface forming algorithm based on the bilinear interpolation is studied. And then, the continuous $L_{d,q}$ surfaces can be formed by identifying only a few data. The detailed explanation of the algorithm is presented as follows.

First, as shown in Fig. 4(a) and (b), the injected dc $i_{d,q}$ combinations are scanned by changing the d*q*-axis current references

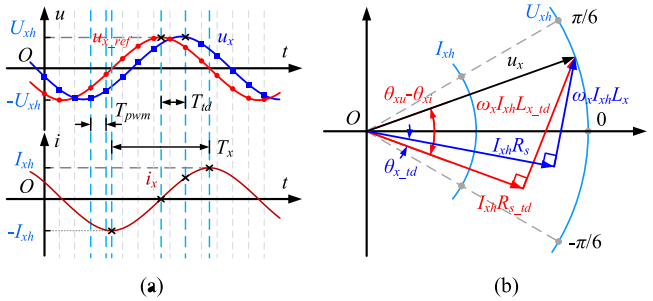

Fig. 5. Influence of digital delay effect on inductance identification. (a) Digital delay effect in the HF signal injection process. (b) Equivalent impedance vectors affected by digital delay.

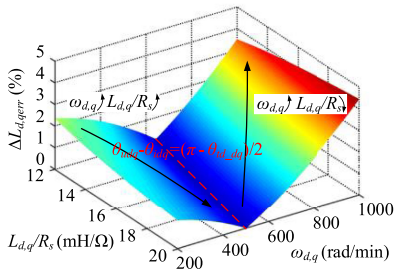

Fig. 6. Relationship between inductance identification time delay error and $L_{d,q}/R_s$ and $\omega_{d,q}$.

i_{d,q_ref}, the expression of which can be expressed by

$$\begin{cases} i_{d\_\mathrm{ref}}(l) = lI_{\max\_d}/l_0 & l = 1, 2, \ldots, l_0 \\ i_{q\_\mathrm{ref}}(k) = kI_{\max\_q}/k_0 & k = 1, 2, \ldots, k_0 \end{cases} \tag{8}$$

where, $I_{\max\_d,q}$ are the preset maximum values of the injected $i_{d,q}$. l and k are the count variables for current scanning. The points p_{lk} in Fig. 4(c) are exactly corresponding to the lth and kth current reference i_{d,q_ref} in Fig. 4(a) and (b). Through the whole current scanning process, the identified points can thus cover all saturation states in grid shape, as shown in Fig. 4(c). k_0 and l_0 are the maximum count values for $i_{d,q}$ scanning, and the total number of the identified points can be determined by the product of k_0 and l_0.

Apparently, with the proposed signal injection strategy in (6), the inductance identification data are current-discrete, as shown in Fig. 4, which cannot be directly applied to the machine control under continuous working condition. Hence, a continuous inductance surface forming algorithm is introduced by the bilinear interpolation relying on the limited number of current-discrete data. As presented in (9), $L_{d,q}$ can be seen as a function of $i_{d,q}$. Under an arbitrary point $i_{ds,qs}$ combination, the identified inductance $L_{d,q}$ (i_{ds}, i_{qs}) can be fitted by the four adjacent data points, $L_{d,q}$ (i_{dl}, i_{qk}), $L_{d,q}$ (i_{dl+1}, i_{qk}), $L_{d,q}$ (i_{dl}, i_{qk+1}), and $L_{d,q}$ ($i_{d\ l+1}$, $i_{q\ k+1}$), the derivation process of which is given in the Appendix. In the actual experiment, the sampling numbers of l_0 and k_0 are selected from 5 to 7, where the continuous $L_{d,q}$ surfaces can be satisfactorily generated. The total identification time is within 20 s, as shown in the experimental test of Fig. 10. However, the existing methods often require several times more identified data to form the $L_{d,q}$ surfaces [6], [16]. By applying the bilinear interpolation based inductance surface forming algorithm, the efficiency of the proposed offline inductance identification method is further improved.

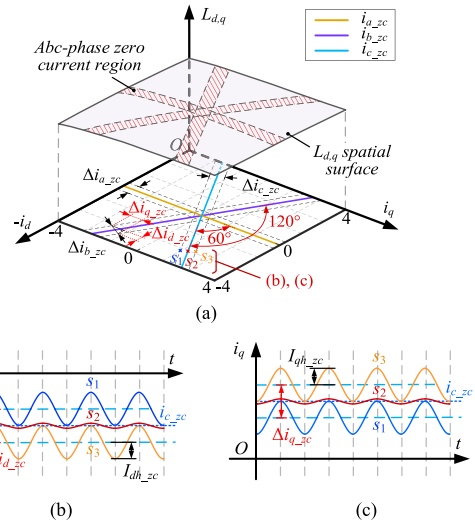

Fig. 7. Zero current zones in *abc* phases and *dq* axes. (a) *abc*-phase zero current zones on $i_{d,q}$ plane. (b) Relationship between width of *abc*-phase ZCZ and amplitudes of HF induced i_d. (c) Relationship between width of *abc*-phase ZCZ and amplitudes of HF induced i_q.

In summary, the advantages of the proposed identification method over the existing voltage equation based methods are as follows. First, the inverter nonlinearity does not need to be compensated in the proposed method. And then, the inductance can be easily calculated without intermediate data storage and complex mathematical operations. Furthermore, the $L_{d,q}$ inductance surfaces can be obtained by fewer data by the bilinear interpolation based surface forming method. The proposed method has better generality and the practicability.

D. Novelty and Advantages of the Proposed Method Compared With the Existing Parameter Identification Methods

In order to present the contributions of the proposed method, in this part, the identification effect of the proposed method

$$\begin{cases} X_{d,qh} = \frac{2}{N_{d,q}} \sqrt{\left(\sum_{n=1}^{N-1} x_{d,qh}(n)\cos(2\pi n/N_{d,q})\right)^2 + \left(\sum_{n=1}^{N-1} x_{d,qh}(n) sin(2\pi n/N_{d,q})\right)^2} \\ \theta_{xd,q} = \arctan\left(\sum_{n=1}^{N-1} x_{d,qh}(n) sin(2\pi n/N_{d,q}) \Big/ \sum_{n=1}^{N-1} x_{d,qh}(n)\cos(2\pi n/N_{d,q})\right) \end{cases} \quad \begin{matrix} X = U, I \\ x = u, i \end{matrix} \tag{7}$$

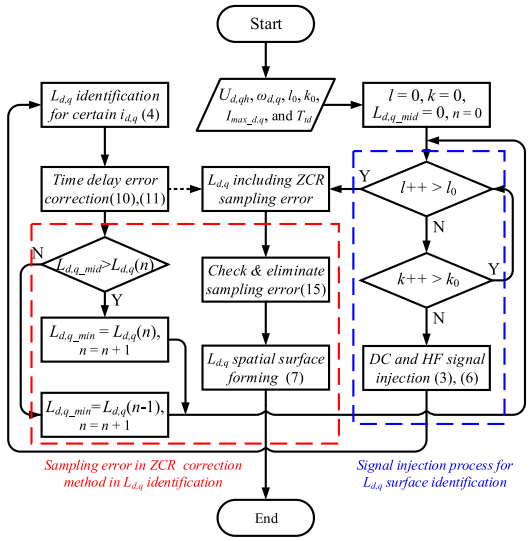

Fig. 8. Flowchart for the proposed $L_{d,q}$ identification method with the correction method of the sampling error in ZCZ.

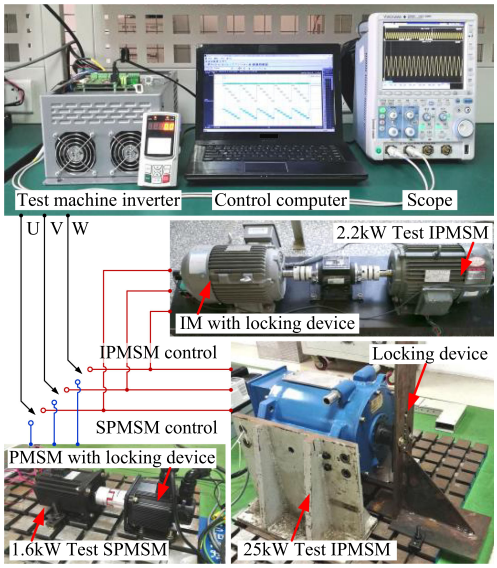

Fig. 9. Test platform with the test 25-kW IPMSM and 1.6-kW SPMSM.

is compared with three widely applied offline identification methods [14], [15], [17] and the online identification method in the authors' previous research [23]. Table I presents the overall differences among the proposed method and the benchmark methods.

The main items in Table I are explained in detail to present the advantages of the proposed method, which are presented as follows.

1) The method in [17] is affected by the inverter nonlinearity error, which is involved in the calculation process. The inverter nonlinearity error also affects the identification results in [14] and [15] since the injected FF signals reduce the signal to noise ratio of the $L_{d,q}$ information. However, the proposed method is immune to inverter nonlinearity error.

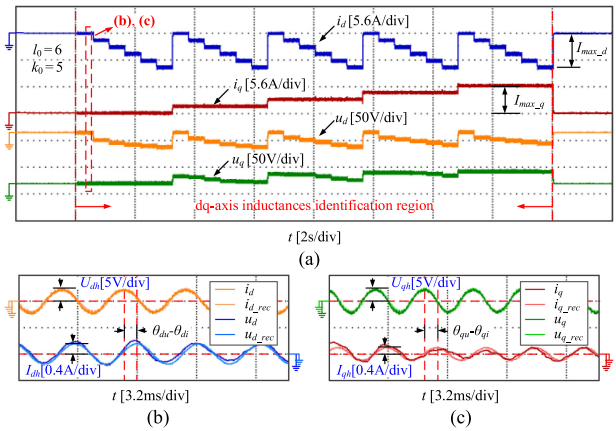

Fig. 10. Experimental waveforms during the whole inductance identification process. (a) Experimental waveforms of $i_{d,q}$ and $u_{d,q}$. (b) Induced i_d and the reconstructed i_{d_rec} by DFT. (c) Induced i_q and the reconstructed i_{q_rec} by DFT.

2) Compared with the proposed method, the conventional methods [14], [15], [17] are resource- and time-consuming for the following reasons. First, the R_s identification and the inverter nonlinearity compensation are required in [17] with a rather complex extra processing. Second, in the voltage equation based methods [6], [17], $L_{d,q}$ need to be calculated by the flux linkage identified in advance. In this case, the extra storage space for the flux linkage data is needed. Finally, for obtaining the continuous inductance surface, the number of the sampling points is increased as much as possible in the conventional methods.
3) The conventional methods without locking the rotor can only be applied within the limited current range. In the proposed method, the rotor is locked making the inductance identification applicable under full current range.
4) The acoustic noise of different methods under certain current level is tested on the 2.2-kW IPMSM by the sound level meter BSWA 308. The acoustic noise of the proposed method and the methods in [15] and [17] is 61.9, 76.9, and 78.2 dB, respectively. It is obvious that the noise of the proposed method is far less than that of the existing methods.

Compared with the online identification method [23], the offline identification does not affect the online control, which is more suitable in some specific applications, such as the high speed machine control, the precision machining and the low noise condition. As for the identification effect, since the saturation degrees of the dq-axis magnetic circuits are determined by $i_{d,q}$ [3], the inductances at offline and online condition under the same current level are the same.

III. Error Analysis and Compensation Strategy in Offline Parameter Identification Process

As the main error sources, the effects of the digital delay and the sampling error in the abc-phase zero current zones on the inductance identification are analyzed in this part, along with the corresponding correction methods [24]–[27].

TABLE I
OVERALL COMPARISON BETWEEN THE PROPOSED METHOD AND EXISTING METHODS IN [14], [15], [17], AND [23]

Contrastive items	Offline method [17]	Offline method [15]	Offline method [14]	Proposed method	Online method [23]
Signal injection	• HF Square voltage injection • Hysteresis control	• FF Sinusoidal voltage injection	• FF Sinusoidal voltage injection • DC current injection	• HF Sinusoidal voltage injection • DC current injection	• HF Sinusoidal voltage injection
Inverter error	• Affected by inverter error	• Affected by inverter error	• Affected by inverter error	• Immune to inverter error	• Immune to inverter error
Computation effort	• Large amount	• Large amount	• Relatively small amount	• Small amount	The online method is • Consuming online control resource • Not suitable for some special application
Allowable identification range	• Limited $i_{d,q}$ range	• Limited $i_{d,q}$ range	• Full $i_{d,q}$ range (only when rotor is locked)	• Full $i_{d,q}$ range (with locked rotor)	
Noise level	• High	• High	• Relatively low	• Low	

FF means fundamental frequency.

A. Effect of Digital Delay on Inductance Identification

In the PMSM digital control system, the actual injected voltage is delayed for 1.5 $T_{\rm pwm}$ relative to the reference voltage $u_{d,q\_{\rm ref}}$ due to the digital delay effect, where $T_{\rm pwm}$ is the PWM period [26], [27]. Since the frequency of the injected sinusoidal voltage is high, digital delay effect cannot be neglected. Taking the time delay error into account, the proposed inductance identification scheme is shown in Fig. 5.

In Fig. 5, the subscript "td" represents the time delay term. In Fig. 5(a), $T_{\rm td}$ is the delayed time, satisfying $T_{\rm td} = 1.5T_{\rm PWM}$. $T_{d,q}$ are the sinusoidal period of the *dq*-axis injected signals. In Fig. 5(b), $\theta_{\rm td}$ is the delayed angle corresponding to $T_{\rm td}$. The mathematical relationship of the delayed angle and the delayed period can be expressed by

$$\theta_{\rm td\_}x = 2\pi\frac{T_{\rm td}}{T_x} = \omega_x T_{\rm td} x = d, q. \tag{10}$$

Based on the previous analysis, $U_{d,qh}$ and $I_{d,qh}$ can be directly obtained by (7), which are not affected by digital delay effect. However, because of the delayed time, the initial phase of the voltage is incorrectly estimated, as shown in Fig. 5(a). The inductive vector $\omega_{d,q}I_{d,qh}L_{d,q\_td}$ would deviate from the actual vector $\omega_{d,q}I_{d,qh}L_{d,q}$, as shown in Fig. 5(b). In this case, the $L_{d,q}$ are then wrongly identified. Considering the digital delay effect, the inductance identification error is obtained by combining (6) and (10), which can be expressed by

$$\begin{aligned}\Delta L_{x\rm err} &= \tfrac{L_x - L_{x\rm err}}{L_x} \\ &= {\rm Abs}\left(\frac{\sin\left(tan^{-1}(\omega_x L_x/R_s)+\theta_{td\_x}\right)}{\sin(tan^{-1}(\omega_x L_x/R_s))} - 1\right) x = d, q.\end{aligned} \tag{11}$$

Given that the delayed time $T_{\rm td}$ is constant for certain $T_{\rm PWM}$, $\Delta L_{d,q\rm err}$ can be regarded as a function of the injection angle frequency $\omega_{d,q}$ and the time constant $L_{d,q}/R_s$, as shown in Fig. 6. It is presented that when $\omega_{d,q}$ and $L_{d,q}/R_s$ satisfy $\theta_{ud,q}$ - $\theta_{id,q} = (\pi - \theta_{\rm td\_}{}_{d,q})$ / 2, the inductance error caused by digital delay effect is 0. Since the PMSM parameters generally change in a relatively small range [23], the influence of $L_{d,q}/R_s$ on inductance identification is small compared with that on $\omega_{d,q}$, as shown in Fig. 6.

Seeing that the time delay error can be expressed by the period error in (10), the delay angle $\theta_{\rm td}$ can be directly compensated in the calculation process in (6), which is shown as follows:

$$L_x = \frac{U_{xh}}{\omega_x I_{xh}} \sin\left(\theta_{ux} - \theta_{ix} - \theta_{td\_x}\right) x = d, q. \tag{12}$$

Furthermore, considering the relationship among the time delay error and $L_{d,q}/R_s$ and $\omega_{d,q}$ in Fig. 6, the digital delay effect can be directly avoided by the injecting signals, whose frequencies are selected near the red line of Fig. 5, shown as follows:

$$\omega_x \approx \frac{\theta_{\rm td\_}x}{T_{\rm td}} = \frac{\pi - 2(\theta_{ux} - \theta_{ix})}{T_{\rm td}} x = d, q. \tag{13}$$

The compensation method in (12) is more general, and the compensation method in (13) needs to be selected properly to verify whether the injection frequencies $\omega_{d,q}$ meet the injection requirements given in Section II-B.

B. Effect of Sampling Error in abc-Phase Zero Current Zones on Inductance Identification

The parasitic capacitance effect leads to a large equivalent resistance in the machine circuit in the *abc*-phase ZCZs [16]. Therefore, under HF sinusoidal voltage injection, the amplitudes of HF induced currents in ZCZ are greatly decreased, which reduces the signal-to-noise ratio for the signal sampling to a large extent. The sampling error is then amplified, resulting in the extraction error of $U_{d,qh}$, $I_{d,qh}$, $\theta_{d,qu}$, and $\theta_{d,qi}$ in (7), and eventually the inductance identification error [18]. It worth mentioning that the sampling error, as the inherent property of the voltage source inverter, can hardly be completely eliminated.

In this situation, a correction method is studied. First, the *abc*-phase ZCZs should be determined, where the injected dc $i_{d,q\_{\rm ref}}$ are to determine the abc-phase zero current lines, around which the injected HF voltages determine the width of the ZCZ.

$$\begin{aligned}L_x(i_{ds}, i_{qs}) = (L_x(i_{dl}, i_{qk}) + (L_x(i_{dl}, i_{qk+1}) - L_x(i_{dl}, i_{qk}))\tfrac{i_{qs}-i_{qk}}{i_{qk+1}-i_{qk}})(1 - \tfrac{i_{ds}-i_{dl}}{i_{dl+1}-i_{dl}}) \\ +(L_x(i_{dl+1}, i_{qk}) + (L_x(i_{dl+1}, i_{qk+1}) - L_x(i_{dl+1}, i_{qk}))\tfrac{i_{qs}-i_{qk}}{i_{qk+1}-i_{qk}})\tfrac{i_{ds}-i_{dl}}{i_{dl+1}-i_{dl}}\end{aligned} x = d, q \tag{9}$$

In the $i_{d,q}$ plane, the *abc*-phase zero current can be expressed as

$$\begin{cases} i_{a\_zc} = i_{d\_\mathrm{ref}}\cos(\theta_e) - i_{q\_\mathrm{ref}}\sin(\theta_e) = 0 \\ i_{b\_zc} = i_{d\_\mathrm{ref}}\cos(\theta_e - \frac{2\pi}{3}) - i_{q\_\mathrm{ref}}\sin(\theta_e - \frac{2\pi}{3}) = 0 \\ i_{c\_zc} = i_{d\_\mathrm{ref}}\cos(\theta_e + \frac{2\pi}{3}) - i_{q\_\mathrm{ref}}\sin(\theta_e + \frac{2\pi}{3}) = 0 \end{cases} \tag{14}$$

where the initial rotor position θ_e can be at any value, which is obtained by the sensorless detection method before the offline identification process.

For the convenience of readers' understanding, the a axis in (14) is set to be aligned with the d-axis (θ_e equal to 0°), and the distribution of *abc*-phase zero current in $i_{d,q}$ plane is shown in Fig. 7. The angles between zero current lines are 60°. As shown in Fig. 7(a), the width of the abc-phase ZCZ Δi_{abc_zc} can be determined by the width of the corresponding *dq*-axis ZCZ $\Delta i_{d,q\_zc}$, the mathematical expression of which is as follows:

$$\Delta i_{abc\_zc} = \sqrt{(\Delta i_{d\_zc})^2 + (\Delta i_{q\_zc})^2}. \tag{15}$$

Fig. 7 shows the relationship between Δi_{abc_zc} and the width of the induced *dq*-axis current $\Delta i_{d,q\_zc}$. It can be seen that the sampling error in ZCZ mainly affects the *dq*-axis current region containing the abc-phase zero currents, as the space between line s_1 and line s_3. The induced HF current should be away from the abc-phase zero currents to avoid the sampling error. Hence, $\Delta i_{d,q\_zc}$ is about twice the amplitude of sinusoidal current I_{d,qh_zc}, as shown in Fig. 7(b) and (c). However, $\mathrm{Id}_{,qh\_zc}$ is varying with the $L_{d,q}$ under different $i_{d,q}$ combinations, which complexifies the following error correction process. In order to simplify the correction process, a certain value, noted as $I_{d,qh\_\max}$, is taken to determine the ZCZ, which is greater than or equal to the maximum I_{d,qh_zc}, as shown in (14)

$$\Delta i_{x\_zc} = 2I_{xh\_zc} \le 2I_{xh\_\max} x = d, q. \tag{16}$$

$I_{d,qh\_\max}$ can be determined by (17), where the minimum inductance $L_{d,q\_\min}$ is chosen and the inverter nonlinearity is ignored. In this case, the $I_{d,qh\_\max}$ can be ensured larger than I_{d,qh_zc} under all $i_{d,q}$ combinations. $L_{d,q\_\min}$ can be obtained via a comparison operation process by scanning the real-time data I_{d,qh_plk}

$$\begin{aligned} I_{xh\_\max} &= \sqrt{U_{xh}/((\omega_x L_{x\_\min})^2 + {R_s}^2)} \\ &\ge \sqrt{U_{xh}/((\omega_x L_x)^2 + (R_s + R_{\mathrm{inv}})^2)} = I_{xh\_plk} \end{aligned} \quad x = d, q. \tag{17}$$

During the identification process, the resistance R_s can be easily identified by [16] and [18]. The detailed offline inductance identification process is shown in Fig. 8, together with the identification process of the width of ZCZ.

Because the amplitude of the injected HF sinusoidal voltage is only 0.01 p.u., $I_{d,qh\_\max}$ are generally small, along with Δi_{abc_zc}. As the result, the inductance identification data affected by the ZCZ sampling error is low-proportion to the whole inductance data, which is proved by the experimental results of Fig. 12. For correcting the sampling error, it should be checked whether the identified data are inside ZCZ by (15)–(17). The limited amount of error data can be directly eliminated, and the inductance surface can be formed with the remaining data by (9). The whole process is shown in the red wireframe in Fig. 8.

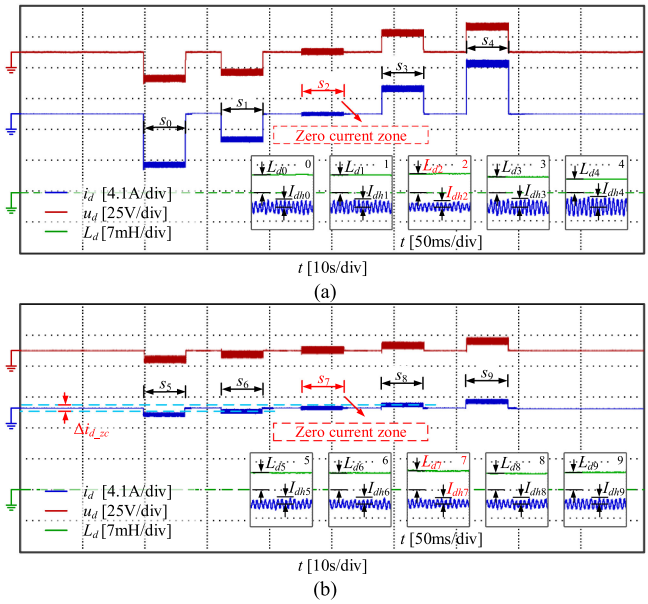

Fig. 11. Error analysis of inductance identification in the ZCZ of d-axis. (a) Amplitudes of induced currents and identified inductances at $\theta_e = 0°$. (b) Amplitudes of induced currents and identified inductances at $\theta_e = 0°$.

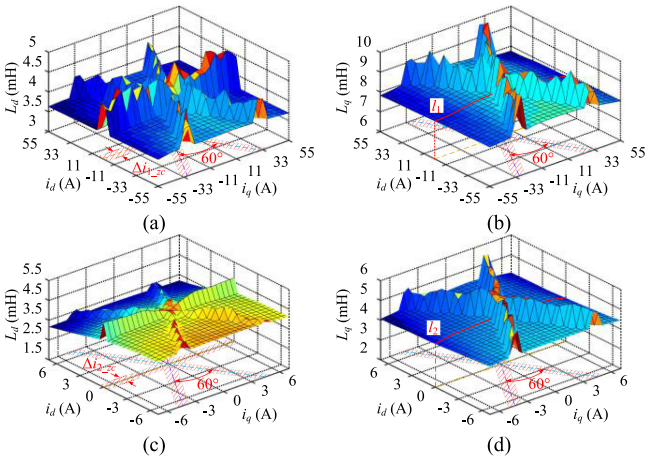

Fig. 12. Experimental results of $L_{d,q}$ including sampling error in ZCZ. (a) L_d of 1.6-kW SPMSM. (b) L_q of 1.6-kW SPMSM. (c) L_d of 25-kW IPMSM. (d) L_q of 25-kW IPMSM.

IV. Experimental Results

The proposed offline inductance identification method is tested on three PMSMs with different structure (SPMSM and IPMSM) to verify the effectiveness. Furthermore, in order to evaluate the generality of the method, the parameters of the three machines are selected quite different on purpose. The rated parameters of test machines are presented in Table II.

The algorithm is implemented by a 22-kW machine drive. The ARM STM32F103 is adopted to execute the parameter identification process. The PWM switching frequency of the inverter is 6 kHz. The overall machine control platform is shown

TABLE II
PARAMETERS OF TEST MACHINES

Parameters	SPMSM	SPMSM	IPMSM
Rated power (kW)	1.6	2.2	25
Rated voltage (V)	200	380	380
Rated current (A)	5	5.6	70
Stator resistance (Ω)	1.38	2.75	0.0456
No load *d*-axis inductance (mH)	4.242	35	0.354
No load *q*-axis inductance (mH)	4.650	64	0.825

TABLE III
AMPLITUDES OF INDUCED CURRENTS AND IDENTIFIED INDUCTANCES IN ZCZ UNDER DIFFERENT REFERENCE CURRENT

Data *n* in Fig.11(a)	0	1	2	3	4
L_{dn} (mH)	4.189	4.181	4.431	3.886	3.651
I_{dhn} (A)	0.348	0.353	0.247	0.434	0.451
Data *n* in Fig.11(b)	5	6	7	8	9
L_{dn} (mH)	4.201	4.174	4.431	4.167	4.173
I_{dhn} (A)	0.265	0.307	0.247	0.321	0.318

TABLE IV
COMPARISON OF ESTIMATION ACCURACY AT DIFFERENT CURRENT LEVELS OF THE PROPOSED METHOD AND THE CONVENTIONAL METHODS

Methods	[17]	[15]	[14]	proposed method
$i_{d,q}$=0	16.5%	21.3%	9.1%	4.9%
$i_{d,q}$=0.5p.u.	2.1%	3.5%	0.5%	1.5%

in Fig. 9, where the rotor shaft is locked during the identification process. In order to prove the reliability of the proposed method, the parameter identification methods in [17] and [23] are adopted as the verification.

Taking 1.6-kW motor as an example, the waveforms of the injected $u_{d,q}$ and the induced $i_{d,q}$ during the whole offline inductance identification process are shown in Fig. 10. It is well presented that the injected signals are composed of both dc currents and the additional HF sinusoidal voltages. In Fig. 10(a), the *dq*-axis dc currents are scanned under the varying i_{d,q_ref} according to (8), where $I_{\max\_d,q}$ are chosen as 5.6 and 7.2 A, respectively, which are larger than the rated current. l_0 and k_0 are chosen to be 5 and 6. The frequencies of the injected HF *dq*-axis voltages are selected as 300 and 375 Hz to decouple the $L_{d,q}$ identification between dq axes. The amplitudes of $U_{d,qh}$ are selected as 0.01 p.u. Considering the actual online PMSM operation condition, it would be enough only to identify the inductance under the current combination of $i_d \leq 0$ and $i_q \geq 0$.

In Fig. 10(b) and (c), $u_{d,q}$ and $i_{d,q}$ are shown in detail. u_{d,q_rec} and i_{d,q_rec} are the reconstructed waveforms with the amplitude and phase extracted by (7), aiming to verify the signal processing effect. It can be seen that, due to the inverter nonlinearity, the injected signals contain harmonics, especially the induced $i_{d,q}$ [23]. However, the harmonics are well eliminated in u_{d,q_rec} and i_{d,q_rec}, which proves the high extraction accuracy of $U_{d,qh}$, $I_{d,qh}$, $\theta_{d,qu}$, and $\theta_{d,qi}$. By applying the proposed signal injection strategy, the whole identification process can be completed within 20 s, as shown in Fig. 10(a). The inductance surface can be obtained by a limited amount of the identified data, which is presented in Figs. 12 and 16.

In Fig. 11, the amplitude of the injected voltage U_{dh} is kept 0.01 p.u. In Fig. 11(a), the amplitudes of induced currents I_{dh0}-I_{dh4} and the identified inductance L_{d0}–L_{d4} are presented under i_{d_ref} varying from −1.4 to 1.4 p.u. with an increment of 0.7 p.u., corresponding to the sampling area s_1–s_5. Generally, the identified inductance L_d should increase with the decrease of current, and the amplitude of the current I_{dh} should decrease simultaneously [16]. However, with the sampling error in ZCZ, I_{dh2} is the smallest due to the large resistance of the inverter nonlinearity. The influence of sampling error is then amplified at such small current amplitude, making L_{d2} inaccurate [18]. As shown in Table III, except L_{d2}, the values of inductance are proved correct right by experiments, along with its changing trend of $L_{d0} > L_{d1} > L_{d3} > L_{d4}$ with $I_{dh0} < I_{dh1} < I_{dh3} < I_{dh4}$.

In Fig. 11(b), s_5–s_9 correspond to the i_{d_ref} varying from −0.2 to 0.2 p.u. with an increment of 0.1 p.u. The results in Table III show that, among all the test data, only L_{d7} is evidently affected by the sampling error in ZCZ. Given that the range of i_{d,q_ref} narrowed in Fig. 11(b), ΔI_{d_zc} is approximately equivalent to twice the maximum amplitude of HF induced current $I_{d,qh\_\max}$, which confirms the analysis in Section III-B. It is also proved that the inductance identification data affected by the sampling error in ZCZ is low-proportion to the whole inductance data, which is also illustrated in Fig. 12.

Taking θ_e equal to 0° as an example, Fig. 12 presents the inductance identification results containing the sampling error in ZCZ of the 1.6-kW SPMSM and the 25-kW IPMSM. The identified inductance results near 0°, 60°, and 120° at $i_{d,q}$ plane are apparently distorted. Considering the analysis in Section III-B, it is confirmed that the sampling error in the *abc*-phase ZCZs does affect the $L_{d,q}$ identification. And, the width of the zero current zones Δi_{1_zc} and Δi_{2_zc} are 0.78 and 10 A for 1.6 and 25 kW PMSM, which are also verified by the the identification process in Fig. 12. Through the experimental results, the amount of the error data in the red dashed area is only a small portion of the whole data in $i_{d,q}$ plane, which makes it reasonable to directly eliminate the error data, and form the inductance surface with the remaining data by (9). It is worth mentioning that L_q at $i_d = 0$ ($i_a = 0$) is not affected by the sampling error, as l_1 and l_2 shown in Fig. 12(b) and (d). The reason is that the *a*-phase currents and voltages at θ_e are equal to 0°, including the sampling errors in *a*-phase, are not involved at all in the L_q identification.

For further proving the effect of the sampling error in ZCZ. The estimation accuracy of three more existing methods at different current levels is presented in Table IV through the experiments. In those methods, the sampling error in ZCZ has not been considered. In Table IV, two different current states are applied, where the sampling error in ZCZ is relatively serious at $i_{d,q} = 0$ and the sampling error in ZCZ does not exist at $i_{d,q} = 0.5$ p.u.

It is shown in Table IV that the estimation accuracy is acceptable at relatively high current level for four methods. However, at low current level, the estimation accuracy of the conventional methods is low. According to the comparison with the existing pieces of literature, the compensation of the sampling error in ZCZ is necessary.

TABLE V
COMPARISON BETWEEN THE PROPOSED METHOD AND THE CONVENTIONAL SQUARE WAVE INJECTION BASED METHODS IN COMPUTATION COMPLEXITY OF ONE IDENTIFICATION POINT

Method	Clock cycles in each PWM period	Minimum calculation period	Overall calculation period (10 times)	Advantages of the proposed method
Method in [6], [17]	• 300 clock cycles in each PWM period	• 1 square wave injection period	• 10 square wave injection periods	• The clock cycles taken in each PWM period can be reduced on average
Proposed method	• 200 clock cycles for DFT data sampling • 600 clock cycles for DFT calculation	• 1 sinusoidal wave injection period	• Less than 10 sinusoidal wave injection periods due to the overlap	• The identification period can be reduced by the overlap of the sampling points

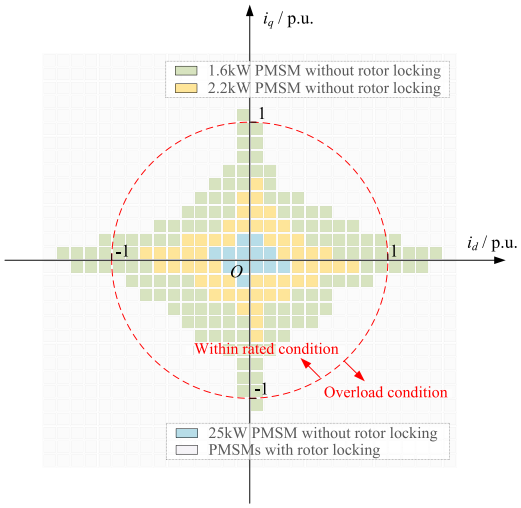

Fig. 13. Allowable identification current range of additional 2.2-kW PMSM, 1.6-kW SPMSM, and 25-kW IPMSM with/without rotor locking.

The allowable identification current ranges of the proposed method and conventional methods are investigated in Fig. 13. In the conventional methods [14], [15], [17], the rotor is not locked. However, the rotor will inevitably rotate when the injected current is relatively high, which limits the allowable identification current range. In Fig. 13, the experiments of the conventional method [17] are carried out to present the maximum *dq*-axis current ranges of the test machines within 10° rotor rotation. As shown in Fig. 13, when the rotor is not locked, the rotor can be kept in standstill at low *dq*-axis current, but the rotation occurs at large current. In the experiments, it is prevailed that the machine with higher rated power has relatively smaller identification range. In the proposed method, the rotor is locked, making the $L_{d,q}$ identification applicable under full current range. Hence, for better achieving the general-purpose offline $L_{d,q}$ identification under full operation condition, the rotor locking is a reliable treatment.

In the conventional square wave injection based methods, the injection frequency is defined by the hysteresis control [6], [17], as the injection period $T_k - T_{k+3}$ shown in Fig. 14, which is variable for different $i_{d,q}$ injection. The $L_{d,q}$ identification is realized in at least one square wave injection period. The *dq*-axis flux linkage $\psi_{d,q}$ need to be stored at the extreme points of the flux linkage waveform.

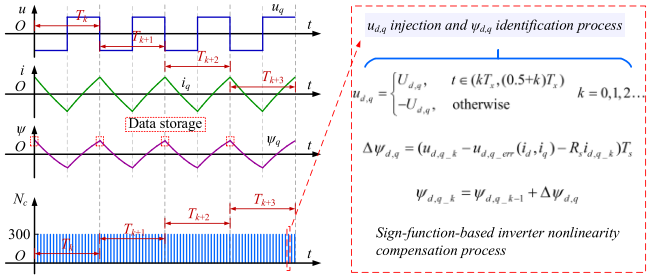

Fig. 14. $L_{d,q}$ identification process of conventional methods [6], [17] and clock cycles during signal injection.

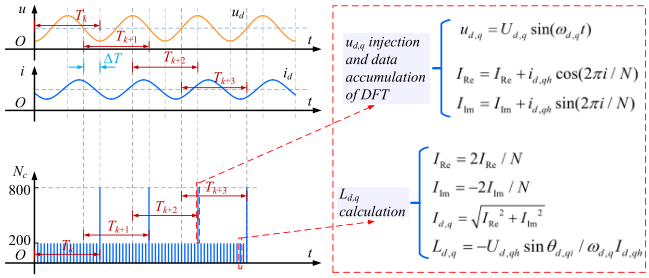

Fig. 15. $L_{d,q}$ identification process of the proposed method and clock cycles during signal injection.

The $L_{d,q}$ calculation in the proposed method is realized by DFT, the process of which is illustrated in Fig. 15. The minimum period of the DFT calculation is one HF sinusoidal injection period. As $T_k - T_{k+3}$ shown in Fig. 15, the overlap of the sampling points between two adjacent injection periods can be achieved in the sinusoidal waveform, where ΔT is the period of the overlapping data, satisfying $0 \le \Delta T \le T_{d,q}$.

The computational time of two methods is presented in Table V, where the average $L_{d,q}$ during ten identification times is taken, and the clock cycles (N_c) in the whole calculation process is taken. It can be concluded that compared with the conventional methods, the proposed method is more lightweight in terms of computation.

In order to verify the effectiveness of the identified $L_{d,q}$, the conventional offline parameter identification method in [17] is applied as the comparison. Meanwhile, the value of $L_{d,q}$ identified by the online method [23] is taken as the standard. It can be seen in Fig. 16(a), (c), (e), (g), (i), and (k) that the overall identification results are approximately the same. L_d

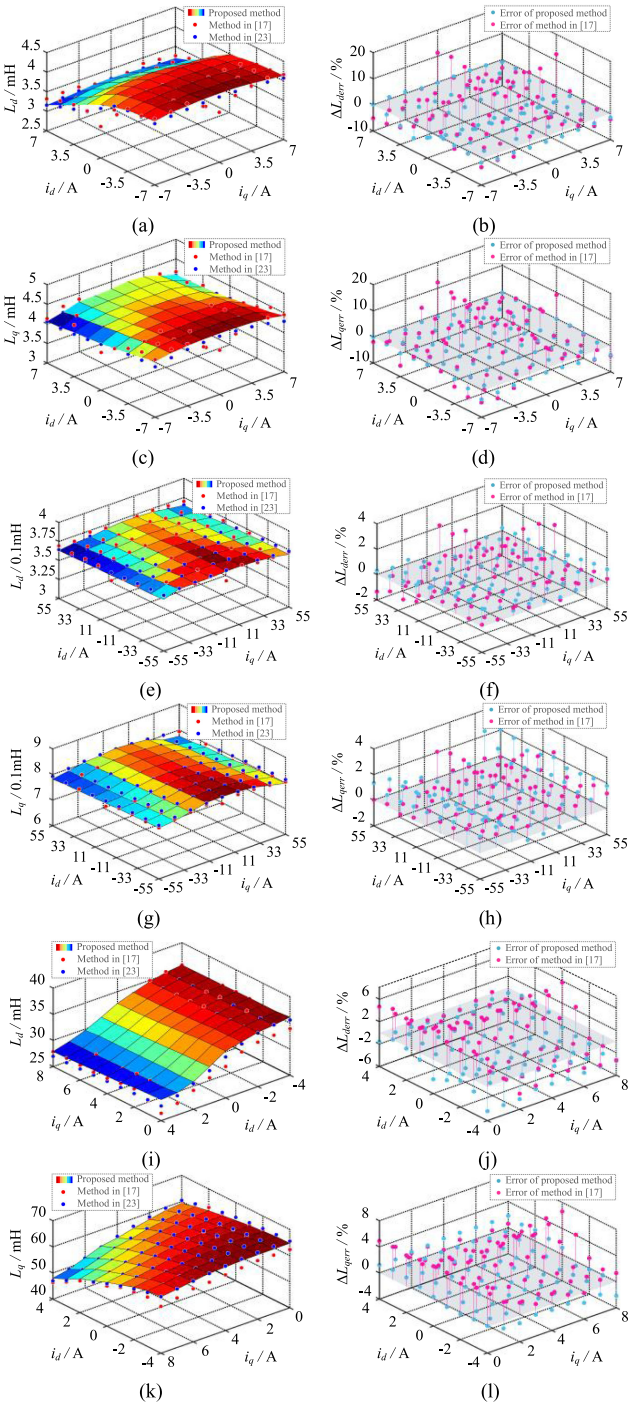

Fig. 16. Experimental results of $L_{d,q}$ and the comparisons with methods in [17] and [23]. (a) L_d of 1.6-kW SPMSM. (b) L_d error of 1.6-kW SPMSM. (c) L_q of 1.6-kW SPMSM. (d) L_q error of 1.6-kW SPMSM. (e) L_d of 25-kW IPMSM. (f) L_d error of 25-kW IPMSM. (g) L_q of 25-kW IPMSM. (h) L_q error of 25-kW IPMSM. (i) L_d of 2.2-kW SPMSM. (j) L_d error of 2.2-kW SPMSM. (k) L_q of 2.2-kW SPMSM. (l) L_q error of 2.2-kW SPMSM.

and L_q decrease with the increasing i_q, and increase with the decreasing i_d due to the magnetic saturation and cross coupling [16]. The unsaturated L_d and L_q values are 4.26 and 4.52 mH for 1.6-kW SPMSM, 0.359 and 0.810 mH for 25-kW IPMSM, 37 and 65 mH for 2.2-kW IPMSM, which are consistent with the nameplate values. Fig. 16(b), (d), (f), (h), (j), and (l) present that the identification error of the proposed method compared with the standard value is smaller than that of the method in [17].

The maximum errors of the experimental results are summarized in Table VI. The identification error of $L_{d,q}$ for three test machine is less than 6%. The accuracy and effectiveness can be then verified.

TABLE VI
MAXIMUM IDENTIFICATION ERRORS OF EXPERIMENTAL RESULTS IN FIG. 16

Identification error	proposed method L_d	proposed method L_q	method in [17] L_d	method in [17] L_q
1.6kW SPMSM	5.7%	3.8%	12.4%	12.2%
25kW IPMSM	1.6%	2.3%	3.6%	3.1%
2.2kW SPMSM	4.3%	2.2%	5.7%	6.6%

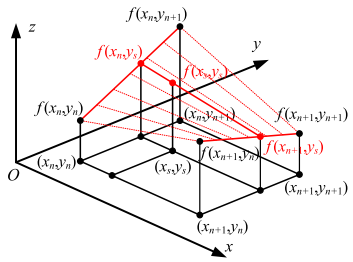

Fig. 17. Schematic diagram of the bilinear interpolation.

V. CONCLUSION

In this article, a new offline inductance identification method based on the equivalent inductance model is proposed. Compared with the existing methods, the equivalent resistance of the inverter nonlinearity is not contained in the inductance identification process, which need not be considered at all in the proposed method. Hence, the identification process can be greatly simplified and the identification efficiency can be improved. Meanwhile, the proposed inductance identification method estimates inductance without storing intermediate data or operating complex mathematical calculation. Furthermore, with the introduced inductance surface forming algorithm based on the bilinear interpolation, the inductance surface can be obtained by only a few identification data. The digital delay and sampling error in zero current zone are well analyzed and corrected, which improves the identification accuracy. The experimental results prove the generality and effectiveness of the proposed method.

APPENDIX

The bilinear interpolation can be used to generate the continuous surface from discrete data points. For the function $z = f(x, y)$, the function value z of any point can be obtained by the four adjacent data points in rectangular arrangement.

As shown in Fig. 17, taking an arbitrary data point with the coordinate (x_s, y_s) as example, the function value $f(x_s, y_s)$ can be calculated by the function values of the four adjacent data points at (x_n, y_n), (x_{n+1}, y_n), (x_n, y_{n+1}), (x_{n+1}, y_{n+1}). In the bilinear interpolation, the linear interpolation is carried out twice in both

x-axis and y-axis, which are presented as follows:

$$f(x_n, y_s) = f(x_n, y_n) + (f(x_n, y_{n+1}) - f(x_n, y_n))\frac{y - y_n}{y_{n+1} - y_n} \tag{A1}$$

$$f(x_{n+1}, y_s) = f(x_{n+1}, y_n) + (f(x_{n+1}, y_{n+1}) - f(x_{n+1}, y_n))\frac{y - y_n}{y_{n+1} - y_n} \tag{A2}$$

$$f(x_s, y_s) = f(x_n, y_s) + (f(x_{n+1}, y_s) - f(x_n, y_s))\frac{x - x_n}{x_{n+1} - x_n}. \tag{A3}$$

REFERENCES

[1] G. Wang, M. Valla, and J. Solsona, "Position sensorless permanent magnet synchronous machine drives—A review," *IEEE Trans. Ind. Electron.*, vol. 67, no. 7, pp. 5830–5842, Jul. 2020.

[2] G. Wang, R. Yang, and D. Xu, "DSP-based control of sensorless IPMSM drives for wide-speed-range operation," *IEEE Trans. Ind. Electron.*, vol. 60, no. 2, pp. 720–727, Feb. 2013.

[3] S. A. Odhano, P. Pescetto, H. A. A. Awan, M. Hinkkanen, G. Pellegrino, and R. Bojoi, "Parameter identification and self-commissioning in AC motor drives: A technology status review," *IEEE Trans. Power Electron.*, vol. 34, no. 4, pp. 3603–3614, Apr. 2019.

[4] S. A. Odhano, R. Bojoi, M. Popescu, and A. Tenconi, "Parameter identification and self-commissioning of AC permanent magnet machines—A review," in *Proc. IEEE Workshop Elect. Mach. Des. Control Diagnosis*, Aug. 2015, pp. 195–203.

[5] M. S. Rafaq and J. Jung, "A comprehensive review of state-of-the-art parameter estimation techniques for permanent magnet synchronous motors in wide speed range," *IEEE Trans. Ind. Informat.*, vol. 16, no. 7, pp. 4747–4758, Jul. 2020.

[6] M. Hinkkanen, P. Pescetto, E. Mölsä, S. E. Saarakkala, G. Pellegrino, and R. Bojoi, "Sensorless self-commissioning of synchronous reluctance motors at standstill without rotor locking," *IEEE Trans. Ind. Appl.*, vol. 53, no. 3, pp. 2120–2129, May/Jun. 2017.

[7] G. Pellegrino, B. Boazzo, and T. M. Jahns, "Magnetic model self-identification for PM synchronous machine drives," *IEEE Trans. Ind. Appl.*, vol. 51, no. 3, pp. 2246–2254, May/Jun. 2015.

[8] D. Fodorean, L. Idoumghar, M. Brévilliers, P. Minciunescu, and C. Irimia, "Hybrid differential evolution algorithm employed for the optimum design of a high-speed PMSM used for EV propulsion," *IEEE Trans. Ind. Electron.*, vol. 64, no. 12, pp. 9824–9833, Dec. 2017.

[9] S. Nadarajan, S. K. Panda, B. Bhangu, and A. K. Gupta, "Online model-based condition monitoring for brushless wound-field synchronous generator to detect and diagnose stator windings turn-to-turn shorts using extended Kalman filter," *IEEE Trans. Ind. Electron.*, vol. 63, no. 5, pp. 3228–3241, May 2016.

[10] Y. Chen, W. Li, F. Iannuzzo, H. Luo, X. He, and F. Blaabjerg, "Investigation and classification of short-circuit failure modes based on three-dimensional safe operating area for high-power IGBT modules," *IEEE Trans. Power Electron.*, vol. 33, no. 2, pp. 1075–1086, Feb. 2018.

[11] J. Long, M. Yang, Y. Chen, D. Xu, and F. Blaabjerg, "A novel voltage injection based offline parameters identification for current controller auto tuning in SPMSM drives," *Energies*, vol. 13, 2020, Art. no. 3010.

[12] M. Zafarani, E. Bostanci, Y. Qi, T. Goktas, and B. Akin, "Interturn short-circuit faults in permanent magnet synchronous machines: An extended review and comprehensive analysis," *IEEE J. Emerg. Sel. Topics Power Electron.*, vol. 6, no. 4, pp. 2173–2191, Dec. 2018.

[13] X. Wang, Z. Wang, Z. Xu, M. Cheng, W. Wang, and Y. Hu, "Comprehensive diagnosis and tolerance strategies for electrical faults and sensor faults in dual three-phase PMSM drives," *IEEE Trans. Power Electron.*, vol. 34, no. 7, pp. 6669–6684, Jul. 2019.

[14] S. A. Odhano, P. Giangrande, R. I. Bojoi, and C. Gerada, "Self-commissioning of interior permanent-magnet synchronous motor drives with high-frequency current injection," *IEEE Trans. Ind. Appl.*, vol. 50, no. 5, pp. 3295–3303, Sep./Oct. 2014.

[15] S. A. Odhano, R. Bojoi, Ş. G. Roşu, and A. Tenconi, "Identification of the magnetic model of permanent-magnet synchronous machines using DC-biased low-frequency AC signal injection," *IEEE Trans. Ind. Appl.*, vol. 51, no. 4, pp. 3208–3215, Jul./Aug. 2015.

[16] Q. Wang, G. Zhang, G. Wang, C. Li, and D. Xu, "Offline parameter self-learning method for general-purpose PMSM drives with estimation error compensation," *IEEE Trans. Power Electron.*, vol. 34, no. 11, pp. 11103–11115, Nov. 2019.

[17] P. Pescetto and G. Pellegrino, "Automatic tuning for sensorless commissioning of synchronous reluctance machines augmented with high-frequency voltage injection," *IEEE Trans. Ind. Appl.*, vol. 54, no. 5, pp. 4485–4493, Sep./Oct. 2018.

[18] G. Wang *et al.*, "Self-commissioning of permanent magnet synchronous machine drives at standstill considering inverter nonlinearities," *IEEE Trans. Power Electron.*, vol. 29, no. 12, pp. 6615–6627, Dec. 2014.

[19] K. Liu and Z. Q. Zhu, "Position offset-based parameter estimation for permanent magnet synchronous machines under variable speed control," *IEEE Trans. Power Electron.*, vol. 30, no. 6, pp. 3438–3446, Jun. 2015.

[20] G. Wang, Y. Wang, J. Qi, R. Ni, W. Chen, and D. Xu, "Offline inductance identification of PMSM with adaptive inverter nonlinearity compensation," in *Proc. 9th Int. Conf. Power Electron. ECCE Asia*, 2015, pp. 2438–2444.

[21] C. Lai, G. Feng, Z. Li, and N. C. Kar, "Computation-efficient decoupled multiparameter estimation of PMSMs from massive redundant measurements," *IEEE Trans. Power Electron.*, vol. 35, no. 10, pp. 10729–10740, Oct. 2020.

[22] C. Li, G. Wang, G. Zhang, D. Xu, and D. Xiao, "Saliency-based sensorless control for SynRM drives with suppression of position estimation error," *IEEE Trans. Ind. Electron.*, vol. 66, no. 8, pp. 5839–5849, Aug. 2019.

[23] Q. Wang, G. Wang, N. Zhao, G. Zhang, Q. Cui, and D. Xu, "An impedance model-based multiparameter identification method of PMSM for both offline and online conditions," *IEEE Trans. Power Electron.*, vol. 36, no. 1, pp. 727–738, Jan. 2021.

[24] Q. N. Trinh, P. Wang, Y. Tang, L. H. Koh, and F. H. Choo, "Compensation of DC offset and scaling errors in voltage and current measurements of three-phase AC/DC converters," *IEEE Trans. Power Electron.*, vol. 33, no. 6, pp. 5401–5414, Jun. 2018.

[25] J. Lu, Y. Hu, J. Liu, J. Wang, and P. Li, "Fixed-point sampling strategy for estimation on current measurement errors in IPMSM drives," *IEEE Trans. Power Electron.*, vol. 36, no. 5, pp. 5748–5759, May 2021.

[26] G. Zhang, G. Wang, D. Xu, and N. Zhao, "ADALINE-network-based PLL for position sensorless interior permanent magnet synchronous motor drives," *IEEE Trans. Power Electron.*, vol. 31, no. 2, pp. 1450–1460, Feb. 2016.

[27] C. Lian, F. Xiao, J. Liu, and S. Gao, "Analysis and compensation of the rotor position offset error and time delay in field-oriented-controlled PMSM drives," *IET Power Electron.*, vol. 13, no. 9, pp. 1911–1918, Dec./Jul. 2020.

Qiwei Wang received the B.S. and M.S. degrees in electrical engineering, in 2015 and 2017, respectively, from the Harbin Institute of Technology, Harbin, China, where he is currently working toward the Ph.D. degree in power electronics and electrical drives with the School of Electrical Engineering and Automation.

His current research interests include parameter identification technique and PMSM position sensorless control.

Gaolin Wang (Senior Member, IEEE) received the B.S., M.S., and Ph.D. degrees in electrical engineering from the Harbin Institute of Technology, Harbin, China, in 2002, 2004, and 2008, respectively.

In 2009, he joined as a Lecturer with the Department of Electrical Engineering, Harbin Institute of Technology, where he has been a Full Professor of electrical engineering since 2014. From 2009 to 2012, he was a Postdoctoral Fellow with Shanghai Step Electric Corporation, where he was involved in the traction machine control for direct-drive elevators. He has authored or coauthored more than 60 technical papers in journals and conference proceedings. He is the holder of ten Chinese patents. His current research interests include permanent magnet synchronous motor drives, high-performance direct-drive for traction systems, position sensorless control of ac motors, efficiency optimization control of PMSM, and digital control of power converters.

Dr. Wang is a Guest Editor for IEEE TRANSACTIONS ON INDUSTRIAL ELECTRONICS, an Associate Editor for *IEEE Access, IET Electric Power Applications,* and *Journal of Power Electronics*.

Shaobo Liu received the B.S. and M.S. degrees in electrical engineering, in 2018 and 2020, respectively, from the Harbin Institute of Technology, Harbin, China, where he is currently working toward the Ph.D. degree in power electronics and electrical drives.

His current research interests include high efficiency ac–dc converter, PMSM parameter identification technique, and application of GaN power devices.

Guoqiang Zhang (Member, IEEE) received the B.S. degree in electrical engineering from Harbin Engineering University, Harbin, China, in 2011, and the M.S. and Ph.D. degrees in electrical engineering from the Harbin Institute of Technology, Harbin, China, in 2013 and 2017, respectively.

Since then, he has been a Postdoctoral Fellow and a Lecturer with the Department of Electrical Engineering, Harbin Institute of Technology. His current research interests include parameter identification technique, and control of electrical drives, with main focus on sensorless field-oriented control of interior permanent magnet synchronous machines.

Dr. Zhang is an Associate Editor for the *Journal of Power Electronics*.

Dianguo Xu (Fellow, IEEE) received the B.S. degree in control engineering from Harbin Engineering University, Harbin, China, in 1982, and the M.S. and Ph.D. degrees in electrical engineering from the Harbin Institute of Technology (HIT), Harbin, China, in 1984 and 1989, respectively.

In 1984, he joined the Department of Electrical Engineering, HIT, as an Assistant Professor. Since 1994, he has been a Professor with the Department of Electrical Engineering, HIT. He was the Dean of the School of Electrical Engineering and Automation, HIT, from 2000 to 2010, and the Assistant President of HIT from 2010 to 2014. He is currently the Vice President of HIT. He authored or coauthored more than 600 technical papers. His research interests include renewable energy generation technology, power quality mitigation, sensorless vector controlled motor drives, and high-performance PMSM servo system.

Dr. Xu is an Associate Editor for the IEEE TRANSACTIONS ON INDUSTRIAL ELECTRONICS and the *IEEE Journal of Emerging and Selected Topics in Power Electronics*. He is the Chairman of the IEEE Harbin Section.